

# Theoretical and experimental characterization of coherent anti-Stokes Raman scattering microscopy

Ji-Xin Cheng, Andreas Volkmer,\* and X. Sunney Xie

Department of Chemistry and Chemical Biology, Harvard University, 12 Oxford Street, Cambridge, Massachusetts 02138

Received September 3, 2001; revised manuscript received November 26, 2001

We present a systematic characterization of coherent anti-Stokes Raman scattering (CARS) microscopy. CARS signal generation in a heterogeneous sample under a tight-focusing condition is formulated by the Green's function method. The CARS radiation pattern and the forward- and backward-detected CARS signals from a three-dimensional Raman scatterer are calculated. The coherent nature of CARS image formation and its consequences for image contrast and spatial resolution are investigated. Experimental implementations of CARS microscopy with collinearly copropagating and counterpropagating excitation beams, forward and backward data collection, and polarization-sensitive detection are described. Finally, CARS images of unstained live cells with forward detection, epidetection, and polarization-sensitive detection are presented and compared. © 2002 Optical Society of America

OCIS codes: 180.5810, 300.6230, 170.6900, 190.4380.

## 1. INTRODUCTION

Imaging of chemical and biological systems based on various spectroscopic signals is a subject of wide interest. Fluorescence microscopy has been a powerful technique in cell biology<sup>1,2</sup> following the development of various fluorescent probes<sup>2,3</sup> and the achievement of three-dimensional sectioning capability with confocal detection<sup>4</sup> and multiphoton excitation.<sup>5–7</sup> However, this technique has two disadvantages, namely, the photobleaching of fluorescent probes and their perturbation of cell functions.<sup>8</sup> Imaging based on the inherent vibrational properties of molecules provides a direct way of chemically mapping an unstained sample. Infrared (IR) imaging<sup>9</sup> and Raman imaging<sup>10</sup> are two mapping methods that are prevalent in vibrational microscopy. The spatial resolution of IR imaging is limited by the long excitation wavelength used (several micrometers), and IR absorption of water hinders the application of IR imaging to living cells. The shorter excitation wavelength used in Raman imaging avoids these problems. Three-dimensional Raman images with a high spatial resolution were obtained with a confocal Raman microscope.<sup>11</sup> However, this technique necessitates a high average laser power because of the low cross section of Raman scattering and often suffers from the presence of fluorescence background.

The difficulties in spontaneous Raman imaging can be circumvented by multiphoton microscopy based on coherent anti-Stokes Raman scattering (CARS). CARS spectroscopy has become the most well known nonlinear Raman technique<sup>12</sup> since the first systematic study of CARS by Maker and Terhune in 1965.<sup>13</sup> CARS spectroscopy has been extensively reviewed.<sup>14–16</sup> Briefly, CARS is a third-order nonlinear optical process that involves a pump and a Stokes laser beam at frequencies of  $\omega_p$  and

$\omega_s$ , respectively. The CARS signal at the anti-Stokes frequency of  $2\omega_p - \omega_s$  is resonantly enhanced when  $\omega_p - \omega_s$  is tuned to a Raman band, which can be used as the vibrational contrast in CARS microscopy. Other nonlinear optical techniques, such as second-harmonic generation,<sup>17–19</sup> sum-frequency generation,<sup>20</sup> and third-harmonic generation,<sup>21,22</sup> have also been incorporated with scanning microscopy. Among them, sum-frequency generation microscopy also provides vibrational contrast, but this technique is surface sensitive instead of bulk sensitive.

CARS microscopy has several advantages. First, because CARS is a coherent process, the constructive interference of the anti-Stokes radiation makes the CARS signal not only much larger than the spontaneous Raman signal but also directional for a sizable sample, so the collection efficiency is much higher than for spontaneous Raman scattering. Second, because the signal frequency is higher than the excitation frequencies, CARS can be detected in the presence of one-photon-induced fluorescence. Third, because CARS has a quadratic dependence on the pump field's intensity and a linear dependence on the Stokes field's intensity, the signal is generated in a small focal volume under the tight-focusing condition. Tight focusing permits three-dimensional sectioning of thick samples with high spatial resolution, similarly to multiphoton fluorescence microscopy.<sup>5</sup>

Duncan *et al.* constructed the first CARS microscope in 1982.<sup>23</sup> They used two visible dye lasers and a noncollinear beam geometry. The CARS signal was detected in the phase-matching direction by use of a two-dimensional detector. However, the sensitivity of this scheme was limited for the reasons described below. Zumbusch *et al.*<sup>24</sup> reinvigorated CARS microscopy in 1999 by using two tightly focused near-IR laser beams in a collinear ge-

ometry. The anti-Stokes signal was detected in the forward direction. The tight focus reduced the excitation volume and permitted three-dimensional CARS imaging. That research triggered many activities recently.<sup>25–28</sup>

The reason for using a collinear beam geometry in CARS microscopy is as follows: CARS needs to fulfill the phase-matching condition  $|\Delta \mathbf{k}| \cdot l \ll \pi$ , where  $\Delta \mathbf{k} = \mathbf{k}_{\text{as}} - (2\mathbf{k}_p - \mathbf{k}_s)$  is the wave-vector mismatch and  $l$  is the interaction length.  $\pi/|\Delta \mathbf{k}|$  is the coherence length at which the first maximum of signal is obtained. In a collinear geometry with forward detection, the wave-vector mismatch is  $\Delta k = [n_{\text{as}}\omega_{\text{as}} - (2n_p\omega_p - n_s\omega_s)]/c$ , where  $n_j$  and  $\omega_j$  ( $j = p, s, \text{as}$ ) are the refractive index and the frequency, respectively, for the pump, Stokes, and anti-Stokes beams.<sup>15</sup> Noncollinear beam geometries, such as the folded boxcars geometry,<sup>29</sup> were used in CARS spectroscopy to minimize the wave-vector mismatch and maximize the interaction length. However, the phase-matching condition can be fulfilled with a collinear beam geometry in CARS microscopy because of the small interaction length (several micrometers) and the large cone angle of the wave vectors of the excitation beams under the tight-focusing condition.<sup>30</sup> In this case the noncollinear beam geometry is neither advantageous nor necessary. Comparing the recent implementation of CARS microscopy with collinear geometry<sup>24</sup> and with boxcars geometry<sup>25</sup> reveals that the former has superior spatial resolution and image quality.

The major disadvantage of CARS is the presence of a nonresonant background signal that arises from the electronic contributions, which can be enhanced in the presence of two-photon electronic resonance.<sup>31</sup> In fact, the use of visible light in the 1982 study<sup>23</sup> resulted in a large two-photon-enhanced background signal that overwhelmed the resonant vibrational signal. The use of near-IR light in the 1999 study<sup>24</sup> avoided two-photon electronic resonance and significantly increased sensitivity. In the development of CARS spectroscopy several methods, including double resonance interference,<sup>32</sup> pulse-sequenced CARS,<sup>33</sup> and polarization CARS,<sup>34–37</sup> were employed to reduce the nonresonant background.

Recently, much progress has been made toward reducing the nonresonant background in CARS microscopy. It was reported that epidetected CARS microscopy can significantly reduce solvent background and thus improve sensitivity.<sup>38,39</sup> Cheng *et al.* showed that using longer excitation pulses (picosecond instead of femtosecond) not only can improve the spectral resolution but also can increase the ratio of the resonant CARS signal to the nonresonant background.<sup>38</sup> Recently Cheng *et al.* demonstrated that polarization CARS microscopy permits high-sensitivity vibrational imaging by means of efficient suppression of the nonresonant background from both the sample scatterers and the solvent.<sup>40</sup>

There has been a considerable amount of theoretical work on signal generation in CARS spectroscopy with various beam geometries.<sup>30,41–45</sup> In all these studies a homogeneous bulk sample was considered. However, the situation of CARS microscopy is different in several aspects. First, one uses tightly focused beams for which the paraxial approximation breaks down. Second, the sample composed of the objects to be imaged and of the

surrounding solvent medium is heterogeneous. It is therefore desirable to investigate the signal generation of CARS from a three-dimensional sample with tightly focused beams to be able to understand the distinctive features of CARS imaging. Potma *et al.* calculated the forward-detected CARS signal with tightly focused laser beams.<sup>27</sup> However, those authors dealt only with a thick slab sample, which provides inadequate information for understanding the imaging properties of CARS microscopy. Recently we investigated the forward-to-backward scattering ratio of CARS signals as a coherent addition of the radiation from an ensemble of Hertzian dipoles induced by pump and Stokes beams.<sup>39</sup>

For the research reported here we used the Green's function method to calculate the CARS signal from an arbitrary sample generated with tightly focused Gaussian beams. We present the results of our systematic investigation of various experimental configurations with collinearly copropagating and counterpropagating incident beams, forward and backward signal collection, and polarization-sensitive detection. This paper is organized as follows: In Section 2 we present a theoretical description of the tightly focused incident fields and of signal generation and detection in CARS microscopy. In Section 3 we discuss the numerical results. In Section 4 we present the experimental implementations of CARS microscopy. Finally, we summarize our results in Section 5.

## 2. THEORETICAL MODELING

### A. Description of the Tightly Focused Incident Fields

The focusing of a Gaussian beam is usually described within the paraxial approximation, which is valid only with  $\text{NA}/n$  less than 0.5, where NA is the numerical aperture and  $n$  is the refractive index of the medium.<sup>46</sup> In CARS microscopy the pump and Stokes beams are focused into a sample by an objective lens with a high NA. The description by the angular spectrum representation of a tightly focused field was given by Richards and Wolf<sup>47</sup> and was used in the research reported here. A comparison with the calculation under the paraxial approximation is given in Appendix A.

In CARS microscopy, pulsed beams are used to increase the signal. Because the pulse spatial width (0.3 mm for a 1-ps pulse) is much longer than the focal length, the time-dependent field envelope can be neglected and the pump ( $E_p$ ) and the Stokes ( $E_s$ ) fields can be written as

$$E_p(r, t) = E_p(r)\exp(-i\omega_p t) + \text{c.c.}, \quad (1)$$

$$E_s(r, t) = E_s(r)\exp(-i\omega_s t) + \text{c.c.} \quad (2)$$

We assume that both the pump and the Stokes fields are linearly polarized along the  $x$  axis and that they propagate along the  $z$  axis. The two beams are spatially and temporally overlapped and then focused into a medium by a lens with focal length  $f$ , as depicted in Fig. 1. The incident angle, denoted  $\alpha$ , has a maximum,  $\alpha_{\text{max}}$ , that is related to the NA of the lens by  $\alpha_{\text{max}} = \sin^{-1}(\text{NA}/n)$ . We assume that the incident fields have a fundamental Gaussian profile with a beam waist  $w_0$  before the lens. The incident fields assume the following form:

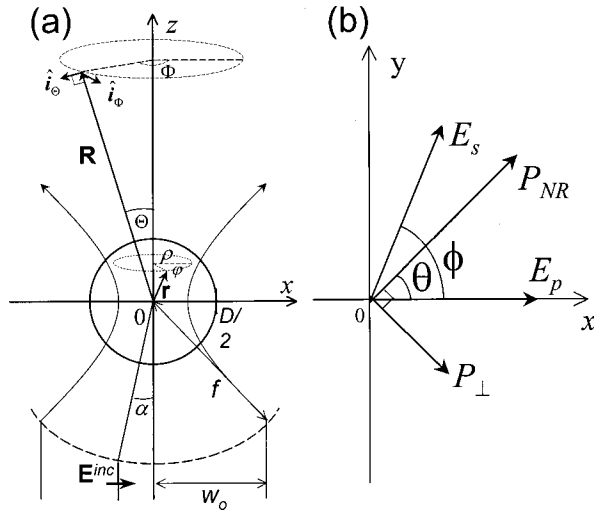


Fig. 1. (a) Illustration of the tight focusing of the incident Gaussian beams and the CARS radiation from a spherical sample with the definitions of the parameters used in the calculation. (b) Illustration of the polarization vectors for the excitation beams and the induced nonlinear polarization.

$$E_j^{inc}(\alpha) = E_{j0} \exp(-f^2 \sin^2 \alpha / w_0^2), \quad (3)$$

where  $j = p, s$  for the pump and the Stokes fields, respectively. The focal field is given in cylindrical coordinates by<sup>47,48</sup>

$$\mathbf{E}_j(\rho, \varphi, z) = \frac{ik_j f \exp(-ik_j f)}{2} \begin{bmatrix} I_{00} + I_{02} \cos 2\varphi \\ I_{02} \sin 2\varphi \\ -i2I_{01} \cos \varphi \end{bmatrix}, \quad (4)$$

with  $\rho = \sqrt{x^2 + y^2}$ . The first, second, and third rows of the vector in Eq. (4) denote the  $x$ ,  $y$ , and  $z$  polarization components, respectively.  $I_{0m}$  is given by

$$I_{0m} = \int_0^{\alpha_{\max}} E_j^{inc}(\alpha) \sin \alpha \sqrt{\cos \alpha} g_m(\alpha) J_m(k_j \rho \sin \alpha) \times \exp(kz \cos \alpha) d\alpha, \quad (5)$$

where  $g_m(\alpha)$  equals  $(1 + \cos \alpha)$ ,  $\sin \alpha$ , and  $(1 - \cos \alpha)$  for  $m = 0, 1, 2$ , respectively.  $J_m$  ( $m = 0, 1, 2$ ) is the Bessel function.  $k_j = 2n_j\pi/\lambda_j$  is the wave-vector amplitude, where  $\lambda_j$  is the laser wavelength. Equations (1)–(3) are also valid for a beam propagating along the  $-z$  direction with  $k_j = -2n_j\pi/\lambda_j$ . Equation (4) shows that the  $y$ - and  $z$ -polarized components result from tight focusing. For a fundamental Gaussian beam under the tight-focusing ( $NA = 1.4$ ) condition,  $\max|\mathbf{E}_y|^2/\max|\mathbf{E}_x|^2 = 0.003$  and  $\max|\mathbf{E}_z|^2/\max|\mathbf{E}_x|^2 = 0.12$  in the  $z = 0$  plane. Moreover, the  $y$ - and  $z$ -polarized fields are zero at the center of the focus. The contributions of  $y$  and  $z$  components to the detected CARS signal are small and are neglected in the following calculations.<sup>49</sup>

Because of the small excitation volume under the high-NA condition, the spectral dispersion of the refractive index of the sample induces little wave-vector mismatch in the collinear beam geometry.<sup>27,30</sup> We can therefore safely neglect index dispersion in calculating the CARS signal. In our modeling we assume no index mismatch between a scatterer and its surrounding medium, and the third-order susceptibilities of the scatterer and

the surrounding medium are assumed to be different. Under this assumption the tightly focused fields described by Eqs. (3)–(5) can be used. The description of the focal field near an index-mismatched planar interface can be found elsewhere.<sup>48,50,51</sup> The calculation of CARS from an index-mismatched interface is feasible but highly complicated. Our model based on the above assumptions captures the essential picture of signal generation in CARS microscopy.

## B. CARS Signal Generation and Detection

CARS microscopy deals with Raman scatterers of arbitrary shape and size. The generation and propagation of the CARS field are governed by the wave equation. The solution to the wave equation of a point source can be obtained by use of Green's function. The signal from a three-dimensional sample is then a linear superposition of the field from each point source inside the sample. In what follows, we begin our formulation with a general form of the wave equation. Gaussian units are used throughout.

The signal field induced by nonlinear polarization in a homogeneous and isotropic medium is governed by the following vector wave equation<sup>52,53</sup>:

$$\nabla \times \nabla \times \mathbf{E}(\mathbf{r}, t) + \frac{n^2}{c^2} \frac{\partial^2 \mathbf{E}(\mathbf{r}, t)}{\partial t^2} = -\frac{4\pi}{c^2} \frac{\partial^2 \mathbf{P}^{NL}(\mathbf{r}, t)}{\partial t^2}. \quad (6)$$

Here  $\mathbf{P}^{NL}(\mathbf{r}, t)$  is the nonlinear polarization,  $n$  is the refractive index of the medium for the signal field, and  $c$  is the vacuum velocity of light. Equation (6) assumes no absorption of the signal field in the medium. The third-order polarization and the generated CARS field at the anti-Stokes frequency of  $\omega_{as} = 2\omega_p - \omega_s$  can be written as

$$\mathbf{P}^{NL}(\mathbf{r}, t) = \mathbf{P}^{(3)}(\mathbf{r}) \exp(-i\omega_{as}t) + \text{c.c.}, \quad (7)$$

$$\mathbf{E}(\mathbf{r}, t) = \mathbf{E}_{as}(\mathbf{r}) \exp(-i\omega_{as}t) + \text{c.c.} \quad (8)$$

Substituting Eqs. (7) and (8) into Eq. (6) and defining  $k_{as}$  as  $n\omega_{as}/c$ , we obtain the wave equation for the CARS field under the slowly varying amplitude approximation:

$$\nabla \times \nabla \times \mathbf{E}_{as}(\mathbf{r}) - k_{as}^2 \mathbf{E}_{as}(\mathbf{r}) = \frac{4\pi\omega_{as}^2}{c^2} \mathbf{P}^{(3)}(\mathbf{r}). \quad (9)$$

By using  $\nabla \times \nabla \times \mathbf{E}_{as}(\mathbf{r}) = -\nabla^2 \mathbf{E}_{as}(\mathbf{r}) + \nabla \nabla \cdot \mathbf{E}_{as}(\mathbf{r})$  and  $\nabla \cdot \mathbf{E}_{as}(\mathbf{r}) = -4\pi \nabla \cdot \mathbf{P}^{(3)}(\mathbf{r})/\epsilon$  with  $\epsilon = n^2$ , we can recast Eq. (9) as

$$\nabla^2 \mathbf{E}_{as}(\mathbf{r}) + k_{as}^2 \mathbf{E}_{as}(\mathbf{r}) = -\frac{4\pi\omega_{as}^2}{c^2} \left( \hat{I} + \frac{\nabla \nabla}{k_{as}^2} \right) \cdot \mathbf{P}^{(3)}(\mathbf{r}), \quad (10)$$

where  $\hat{I}$  is a  $3 \times 3$  unit matrix. The exterior CARS field can be expressed in terms of the scalar Green's function by<sup>54</sup>

$$\mathbf{E}_{as}(\mathbf{R}) = -\frac{4\pi\omega_{as}^2}{c^2} \int_V dV \left( \hat{I} + \frac{\nabla \nabla}{k_{as}^2} \right) G(\mathbf{R} - \mathbf{r}) \cdot \mathbf{P}^{(3)}(\mathbf{r}). \quad (11)$$

Here  $\mathbf{R}(R, \Theta, \Phi)$  denotes the detection position (see Fig. 1) and  $V$  is the volume of the sample. The scalar Green's function for the CARS field is

$$G(\mathbf{R} - \mathbf{r}) = \exp(ik_{\text{as}}|\mathbf{R} - \mathbf{r}|)/4\pi|\mathbf{R} - \mathbf{r}|. \quad (12)$$

In the far field,  $|\mathbf{R}| \gg |\mathbf{r}|$ ,  $|\mathbf{R} - \mathbf{r}|$  can be approximated as  $|\mathbf{R}| - \mathbf{R} \cdot \mathbf{r}/|\mathbf{R}|$ . The spherical components of the CARS field can be written as<sup>55</sup>

$$\begin{aligned} \mathbf{E}_{\text{as}}(\mathbf{R}) = & -\frac{\omega_{\text{as}}^2}{c^2} \frac{\exp(ik_{\text{as}}|\mathbf{R}|)}{|\mathbf{R}|} \int_V dV \exp\left(\frac{-ik_{\text{as}}\mathbf{R} \cdot \mathbf{r}}{|\mathbf{R}|}\right) \\ & \times \begin{bmatrix} 0 & 0 & 0 \\ \cos \Theta \cos \Phi & \cos \Theta \sin \Phi & -\sin \Theta \\ -\sin \Phi & \cos \Phi & 0 \end{bmatrix} \\ & \times \begin{bmatrix} P_x^{(3)}(\mathbf{r}) \hat{i}_R \\ P_y^{(3)}(\mathbf{r}) \hat{i}_\Theta \\ P_z^{(3)}(\mathbf{r}) \hat{i}_\Phi \end{bmatrix} \end{aligned} \quad (13)$$

Here  $\hat{i}_R$ ,  $\hat{i}_\Theta$ , and  $\hat{i}_\Phi$  denote the spherical components of the CARS field. Equation (13) describes the CARS signal from a sample with arbitrary size and shape. It is evident that the far-field CARS signal is a transverse field.

The CARS signal can be collected parvocally in the forward direction by use of a second lens or in the backward direction by the same objective lens. The collected CARS radiation power can be calculated by integration of the field intensity,  $(n_{\text{as}}c/8\pi)|\mathbf{E}_{\text{as}}(\mathbf{R})|^2$ , over the cone angle of the objective lens:

$$P_{\text{CARS}} = \frac{n_{\text{as}}c}{8\pi} \int_{\Theta_1}^{\Theta_2} d\Theta \int_0^{2\pi} d\Phi |\mathbf{E}_{\text{as}}(\mathbf{R})|^2 R^2 \sin \Theta. \quad (14)$$

The integration range of  $[\Theta_1, \Theta_2]$  in Eq. (14) is  $[0, \beta_{\text{max}}]$  for forward detection, where  $\beta_{\text{max}}$  is the cone angle of the collecting lens, and  $[\pi - \alpha_{\text{max}}, \pi]$  for backward detection. Equations (13) and (14) permit the calculation of the detected CARS signal as a coherent addition of the radiation field from the scatterer and that from the solvent. The model described above is generally applicable to any non-linear coherent microscopy.

Assuming that both the pump and the Stokes fields are polarized along the  $x$  axis, the induced polarization,  $\mathbf{P}^{(3)}(\mathbf{r})$ , in Eqs. (9)–(11) has the following form:

$$\mathbf{P}^{(3)}(\mathbf{r}) = 3\chi_{1111}^{(3)}(\omega_{\text{as}}, \mathbf{r}) E_p^2(\mathbf{r}) E_s^*(\mathbf{r}) \hat{i}_x. \quad (15)$$

Unit vector  $\hat{i}_x$  in Eq. (15) indicates that  $\mathbf{P}^{(3)}(\mathbf{r})$  is polarized along the  $x$  axis. The CARS field is then determined by the first column of the matrix in Eq. (13). Pump field  $E_p(\mathbf{r})$  and Stokes field  $E_s(\mathbf{r})$  are described by Eq. (4).  $\chi_{1111}^{(3)}(\omega_{\text{as}})$  is a component of the third-order susceptibility tensor. Away from one-photon electronic resonance,  $\chi_{1111}^{(3)}(\omega_{\text{as}})$  can be obtained from perturbation theory<sup>56</sup>:

$$\begin{aligned} \chi_{1111}^{(3)}(\omega_{\text{as}}) = & \eta_{\text{NR}} + \frac{A_t}{\omega_t - 2\omega_p - i\Gamma_t} \\ & + \frac{A_t}{\omega_t - (\omega_p + \omega_s) - i\Gamma_t} \\ & + \frac{A_t}{\omega_t - 2\omega_s - i\Gamma_t} \\ & + \sum_R \left[ \frac{A_R}{\omega_R - (\omega_p - \omega_s) - i\Gamma_R} \right]. \end{aligned} \quad (16)$$

Here  $t$  denotes two-photon electronic transitions and  $R$  denotes Raman transitions.  $A_j$ ,  $\omega_j$ , and  $\Gamma_j$  ( $j = t, R$ ) represent strength, frequency, and half-width, respectively. The quantity  $\eta_{\text{NR}}$  represents the nonresonant electronic contributions. Using near-IR excitation pulses can prevent two-photon resonance, and the first four terms in Eq. (16) can be combined into a real number, denoted  $\chi^{(3)\text{NR}}$ .

### C. Polarization-Sensitive Detection

The induced polarization in Eq. (15) contains a vibrationally resonant ( $P^R$ ) and a nonresonant ( $P^{\text{NR}}$ ) part, both polarized along the same direction. A general way to suppress the nonresonant background is to utilize the polarization difference between the electronic and the Raman contributions, which can be introduced by use of a pump beam and a Stokes beam of different polarization directions.<sup>34–37</sup> As shown in Fig. 1(b), the pump beam is linearly polarized along the  $x$  axis and the Stokes beam is linearly polarized along an angle  $\phi$  from the  $x$  axis. The  $x$  and  $y$  components of  $P^{\text{NR}}$  can be written as

$$\begin{aligned} P_x^{\text{NR}} &= 3\chi_{1111}^{(3)\text{NR}} E_p^2 E_s^* \cos \phi, \\ P_y^{\text{NR}} &= 3\chi_{1221}^{(3)\text{NR}} E_p^2 E_s^* \sin \phi. \end{aligned} \quad (17)$$

The  $x$  and  $y$  components of the resonant part can be written in a similar way:

$$P_x^R = 3\chi_{1111}^{(3)R} E_p^2 E_s^* \cos \phi, \quad P_y^R = 3\chi_{1221}^{(3)R} E_p^2 E_s^* \sin \phi. \quad (18)$$

Away from electronic resonance, the nonresonant part is linearly polarized with angle  $\theta$  with respect to the  $x$  axis [Fig. 1(b)]:

$$P_{\text{NR}}^{(3)}(\mathbf{r}) = 3\chi_{1111}^{(3)\text{NR}}(\omega_{\text{as}}) E_p^2(\mathbf{r}) E_s^*(\mathbf{r}) \cos \phi / \cos \theta, \quad (19)$$

where angle  $\theta$  is related to  $\phi$  by  $\tan \theta = \rho_{\text{NR}} \tan \phi$ .  $\rho_{\text{NR}} = \chi_{1221}^{(3)\text{NR}}/\chi_{1111}^{(3)\text{NR}}$  is the depolarization ratio for the nonresonant third-order polarization and is equal to 1/3, following Kleinman's symmetry.<sup>57</sup>

The nonresonant part can be suppressed by use of polarization-sensitive detection, for which an analyzer polarizer is placed before the detector to cross the linearly polarized nonresonant signal. The resonant part of the third-order polarization that can be detected through the analyzer has the following form<sup>37</sup>:

$$P_{\perp}^{(3)}(\mathbf{r}) = 3\chi_{1111}^{(3)R}(\omega_{\text{as}}) E_p^2(\mathbf{r}) E_s^*(\mathbf{r}) \cos \phi \sin \theta (1 - \rho_R/\rho_{\text{NR}}). \quad (20)$$

Here  $\rho_R = \chi_{1221}^{(3)R}/\chi_{1111}^{(3)R}$  is the depolarization ratio for the resonant third-order polarization and is equal to the



spontaneous Raman depolarization ratio of the corresponding band.<sup>58</sup> The value of  $\rho_R$  is dependent on the symmetry of the vibrational mode and is in the range of 0–0.75. Equation (20) indicates that the forward-detected polarization CARS intensity depends on the ratio between  $\rho_R$  and  $\rho_{NR}$ . When  $\rho_R = 1/3$ , no resonant signal can be detected. For an anisotropic vibrational mode ( $\rho_R = 0.75$ ), the resonant CARS signal with polarization-sensitive detection is 8% of the resonant signal with parallel-polarized excitation beams.

Assuming that the extinction ratio (measured as the ratio of the maximum to the minimum signals by rotation of the analyzer) is  $r$  for the nonresonant signal, the vibrational contrast with polarization-sensitive detection is

$$P_{\perp}^2/(P_{NR}^2/r) = r[\chi_{1111}^{(3)R}/\chi_{1111}^{(3)NR}]^2(1 - \rho_R/\rho_{NR})^2 \sin^2 \theta \cos^2 \theta. \quad (21)$$

It can be seen that the vibrational contrast is maximized with  $\theta = 45^\circ$ . The optimal value for angle  $\phi$  is then  $71.6^\circ$  according to the relation  $\tan \phi = 3 \tan \theta$ . According to Eq. (21) the signal-to-background ratio (vibrational contrast) can be enhanced by  $r(1 - \rho_R/\rho_{NR})^2/4$  times that with parallel-polarized pump and Stokes beams.

With suppression of the nonresonant background the relative concentration of a specific vibrational oscillator or species can be obtained from the square-rooted image intensity. It should be noted that the linear relation between the concentration and the square-rooted image intensity holds only for a homogeneous sample. The dependence of CARS signals on the shape and orientation of a scatterer at focus (see Subsection 3.B below) may distort the linear relationship.

### 3. NUMERICAL RESULTS AND DISCUSSION

In the following calculation we assume that the waist of the incident beam matches the back aperture of the objective lens (i.e.,  $w_0 = f \sin \alpha_{\max}$ ; see Fig. 1). The refractive index is set to be 1.5. The NA of the objective lenses is assumed to be 1.4, except for the case presented in Subsection 3.D below in which we study the NA dependence of the CARS signal. We also assume that  $\lambda_p = 0.9\lambda_s = 1.1\lambda_{as}$ . For example, if the pump wavelength is 750.0 nm, the CARS wavelength is 681.8 nm and the Raman shift is  $1467.0 \text{ cm}^{-1}$ .

#### A. Tightly Focused Excitation Fields

For a beam propagating along the  $+z$  axis the intensity distribution near the focus is as shown in Fig. 2(a). The lateral intensity profile at  $z = 0$  and the longitudinal profile at  $x = y = 0$  exhibit a FWHM of  $0.4\lambda$  and  $1.0\lambda$ , respectively. Figure 2(b) shows the axial phase shift of the focal field. The plane-wave part [ $\exp(ikz)$ ] is subtracted. A negative phase transition along the  $z$  axis can be seen. This is known as the Gouy phase shift.<sup>46</sup>

It is interesting to discuss the effect of the Gouy phase shift on CARS microscopy. With the tightly focused laser beams, the phase-matching condition for CARS can be approximately revised as  $|\mathbf{k}_{as} - (2\mathbf{k}_p - \mathbf{k}_s)|l - \Delta\phi_g \ll \pi$ .  $\Delta\phi_g = 2\phi_p - \phi_s$  is the phase mismatch induced by the Gouy phase shift of the pump beam ( $\phi_p$ ) and that of the Stokes beam ( $\phi_s$ ) within the interaction length of  $l$ . Un-

der the tight-focusing condition the phase mismatch because of the dispersion of refractive index becomes negligible for forward scattering,  $|k_{as} - (2k_p - k_s)|l \approx 0$ . The Gouy phase shift is  $-\pi$  in the region from  $z = -\lambda$  to  $z = \lambda$  [Fig. 2(b)], however, where most of the signal is generated. Consequently the wave-vector mismatch caused by the Gouy phase shift is  $2\pi/2\lambda_p - \pi/2\lambda_s$ . This value corresponds to a coherence length of  $2\lambda_s\lambda_p/(2\lambda_s - \lambda_p)$ , which is comparable with the axial length of the excitation volume. Therefore a large CARS signal can be obtained from a bulk sample in the forward direction. In contrast, third-order harmonic generation from a bulk medium is canceled under the tight-focusing condition because of a large wave-vector mismatch ( $3\pi/2\lambda$ ) associated with the Gouy phase shift.<sup>52</sup>

#### B. CARS Radiation Pattern

The radiation pattern of CARS is a consequence of the coherent summation of the radiation from an ensemble of coherently induced Hertzian dipoles. The angular distribution of CARS signals under the tight-focusing condition is calculated with Eq. (13). We consider a copropagating beam geometry, i.e., both the pump and Stokes beams propagate along the  $+z$  axis. We set  $R$  as a constant, and the signal is integrated over the angle  $\Phi$ . Figure 3(a) shows the radiation pattern of the CARS signal from spherical scatterers centered at the focus. When diameter  $D$  of the scatterer is much smaller than the pump wavelength, the phase-matching condition is satisfied in

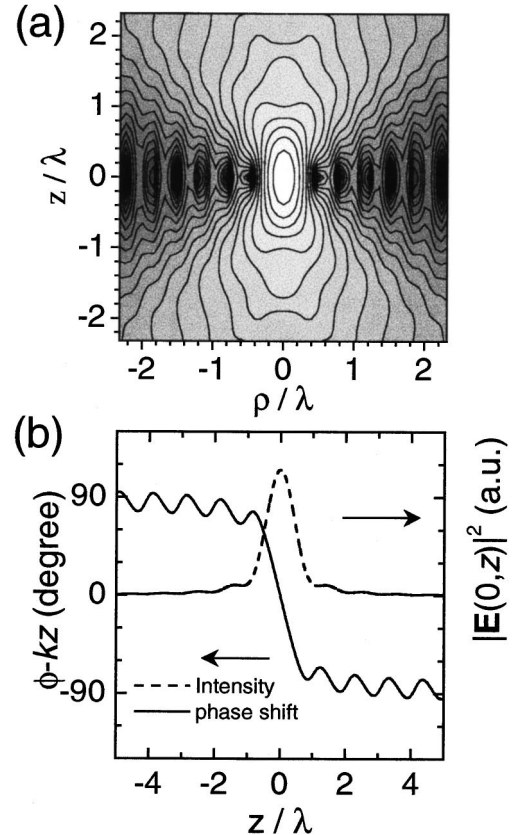


Fig. 2. (a) Intensity distribution on a log scale and (b) axial phase shift of the focal field of a Gaussian beam focused by an objective lens of NA = 1.4.

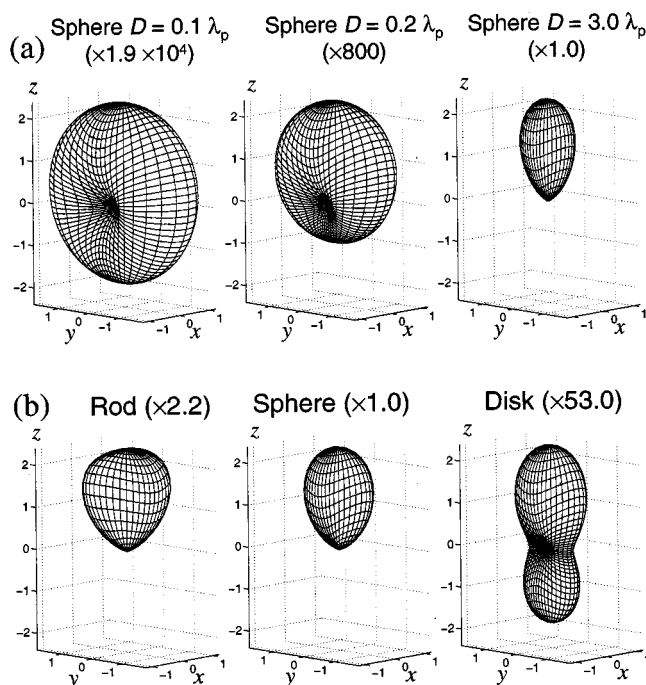


Fig. 3. (a) Far-field CARS radiation pattern from spherical scatterers centered at the focus with different diameters. (b) Far-field CARS radiation pattern from scatterers centered at focus with the same volume but different shapes (rod, sphere, and disk). The rod has a diameter of  $0.2 \lambda_p$  and an axial length of  $2.0 \lambda_p$ . The sphere has a diameter of  $0.78 \lambda_p$ . The disk has a diameter of  $0.89 \lambda_p$  and a thickness of  $0.1 \lambda_p$ . Shown in parentheses are the intensity ratios between samples of different sizes and different shapes. The radiation field is polarized along the  $x$  axis. The signals were calculated with the assumption of tightly focused ( $\text{NA} = 1.4$ ) incident beams copropagating along the  $+z$  axis and polarized along the  $x$  axis.

all directions of  $\mathbf{k}_{\text{as}}$ . Therefore the CARS radiation pattern is symmetric in both the forward and the backward directions, identical to that of a Hertzian dipole. With increasing sample size, the CARS radiation is confined in a small cone angle in the forward direction. The signal from the sample with diameter  $3.0 \lambda_p$  resembles the CARS generation from a bulk medium. Figure 3(a) indicates that the CARS signal from a large scatterer can be efficiently collected with a lens of low NA, whereas collection of the CARS signal from subwavelength samples needs a high-NA lens.<sup>59</sup>

The radiation pattern depends not only on the sample size but also on the sample shape. Figure 3(b) shows the radiation pattern of CARS from a rod sample with diameter  $0.2 \lambda_p$  and length  $2.0 \lambda_p$  along the axial direction, a spherical sample with diameter  $0.78 \lambda_p$ , and a disk sample with diameter  $0.89 \lambda_p$  and thickness  $0.1 \lambda_p$ . Although the three samples have the same volume, their CARS radiation patterns and intensities are quite different. The thin disk sample has a sharp paraxial radiation pattern in both forward and backward directions, whereas the greatest part of the signal from the rod-shaped sample goes forward with a large cone angle than the spherical scatterer. The shape dependence of the signal intensity and the radiation pattern can be used to monitor the tumbling motions or conformation changes of macromolecules with CARS microscopy.

### C. Forward- and Backward-Detected Signals

The forward- ( $+z$ ) and backward- ( $-z$ ) detected CARS signals are calculated from Eq. (14). First we consider a copropagating beam geometry. Figure 4(a) displays the CARS signal as a function of diameter  $D$  of a spherical sample centered at the focus. The forward-detected signal first grows rapidly with the increasing diameter and then becomes saturated when the diameter is larger than  $1.0 \lambda_p$ . The backward-detected (or epidetected) signal exhibits several interesting features. It has the same amplitude as the forward signal when scatterer diameter  $D$  is much smaller than  $\lambda_p$ . The first maximum is reached when diameter  $D$  equals  $0.3 \lambda_p$ . The oscillating behavior with increasing diameter results from the interference effect associated with the large wave-vector mismatch in the backward direction. After the second maximum, the backward signal gradually decreases with increasing diameter. For a  $D = 8.0 \lambda_p$  scatterer the backward signal is  $10^5$  times smaller than the corresponding forward signal. Therefore the epidetection geometry provides a way to image small features embedded in a nonlinear medium,<sup>38,39</sup> which is difficult to do in the forward direction because of the presence of a large forward signal from the surrounding solvent. The epidetected signal from a

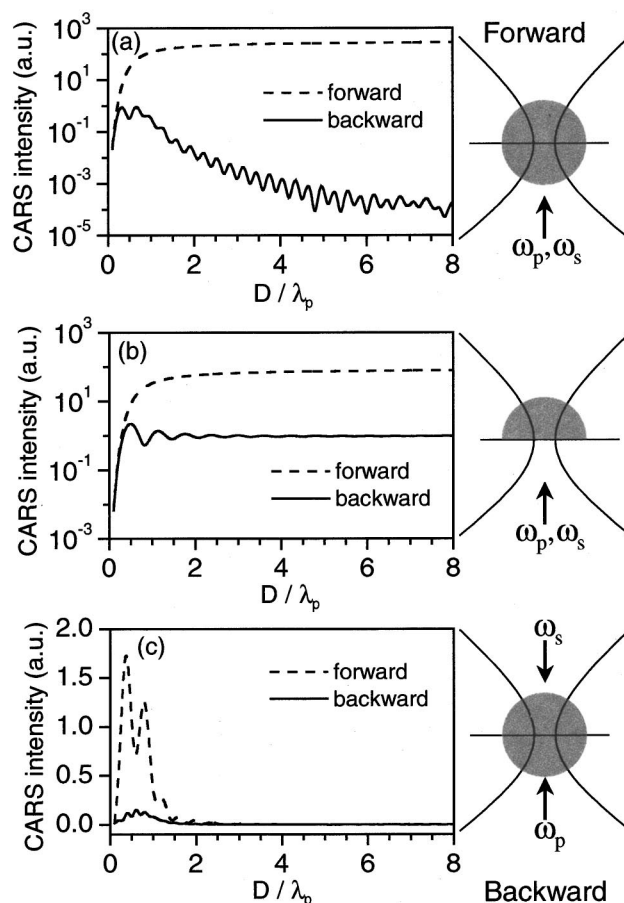


Fig. 4. (a) Forward- and backward-detected signals as a function of the diameter of a spherical sample in a copropagating beam geometry. (b) The same as in (a) but for a hemispherical sample located in the  $z > 0$  region. (c) Forward- and backward-detected signals as a function of the diameter of a spherical sample in a counterpropagating beam geometry.

scatterer with  $\chi_{\text{sca}}^{(3)}$  embedded in a nonlinear medium with  $\chi_{\text{sol}}^{(3)}$  exhibits the same behavior but with an effective sample susceptibility of  $\chi_{\text{sca}}^{(3)} - \chi_{\text{sol}}^{(3)}$ . The signal generation from a small scatterer provides the first contrast mechanism for epidetected CARS microscopy.

Figure 4(b) displays the CARS signal from a hemisphere located in the  $z > 0$  region with its center at the focus. The forward-detected signal displays the same behavior as that for a spherical sample. The maximum of the epidetected signal appears when  $D$  equals  $0.5\lambda_p$ . It can be seen that the epidetected signal from the boundary of such a semi-infinite sample is  $\sim 1.2\%$  of the forward-detected signal. However, our calculation shows that the CARS signal from an interface parallel with the optical axis goes forward and the radiation power is maximized along the optical axis. The signal generation at an interface perpendicular to the optical axis provides the second contrast mechanism for epidetected CARS microscopy.

It should be mentioned that the epidetected CARS at an interface can also arise from a mismatch of the refractive index [ $\text{Re } \chi^{(1)}$ ]. Backward reflection of the forward-going CARS at an index-mismatched interface gives the third contrast mechanism for an epidetected CARS image. In practice, if the excitation beams are not focused on the interface, the backreflected signal is defocused on the detector and can be minimized by the use of confocal detection. For small scatterers, the backreflected signal is negligible compared to the episcattering signal from the scatterer.

One way to avoid a backreflected signal at an interface is to use a counterpropagating beam geometry. We assume that the pump and Stokes beams propagate along the  $+z$  and  $-z$  directions, respectively. As shown in Fig. 4(c), both the forward- ( $+z$ ) and the backward- ( $-z$ ) detected signals evolve with the sample diameter in a similar way as the epidetected signal in the copropagating geometry, whereas the forward signal is much higher than the backward signal. In addition, the maximum of the forward-detected signal in the counterpropagating geometry is approximately twice that of the epidetected signal in the copropagating geometry. The counterpropagating beam geometry provides another way to image small features and thin films embedded in a nonlinear medium by significantly reducing the CARS signal from the bulk medium. It should be noted that CARS signals can also be generated at the interface of two media with different values of  $\chi^{(3)}$  for the counterpropagating geometry.

#### D. Dependence of the CARS Signal on Numerical Aperture

We assume that the focusing and the collection lenses have the same NA. Figure 5 depicts the forward-detected CARS signal from a spherical sample as a function of diameter  $D$  under different NA conditions. It can be seen that the use of a higher-NA objective lens confines the signal generation to a smaller volume and thus improves the spatial resolution. With the same average laser power, the CARS intensity from a subwavelength ( $D < \lambda_p$ ) scatterer can be significantly enhanced by a higher-NA objective. For a bulk sample the signal is slightly higher when a lower-NA objective is used.

#### E. Coherent Image Formation and Spatial Resolution

CARS microscopy is a coherent imaging method. The image intensity is a squared modulus of the coherently superimposed radiation fields from different parts of the sample. Consequently the image profile is no longer the convolution of the objects with the intensity point-spread function of the excitation fields as in the case of fluorescence microscopy.

To understand the coherent nature of CARS imaging, we first consider a model system that contains a spherical Raman scatterer embedded in a nonlinear medium. We assume that the solvent has only a nonresonant contribution,  $\chi_{\text{sol}}^{(3)} = \chi_{\text{sol}}^{(3)\text{NR}}$ , while the scatterer has both resonant and nonresonant components,  $\chi_{\text{sca}}^{(3)} = \chi_{\text{sca}}^{(3)\text{R}} + \chi_{\text{sca}}^{(3)\text{NR}}$ . The nonresonant susceptibilities,  $\chi_{\text{sca}}^{(3)\text{NR}}$  and  $\chi_{\text{sol}}^{(3)\text{NR}}$ , are frequency independent, whereas  $\chi_{\text{sca}}^{(3)\text{R}}$  is described by the last term in Eq. (16). In the calculation we choose  $2\Gamma_R = 9.2 \text{ cm}^{-1}$  and  $A_R/\chi_{\text{sca}}^{(3)\text{NR}} = 2.0 \text{ cm}^{-1}$  based on the CARS spectrum of the  $\omega_R = 1600 \text{ cm}^{-1}$  band of polystyrene (see Fig. 8 below) and  $\chi_{\text{sol}}^{(3)\text{NR}}/\chi_{\text{sca}}^{(3)\text{NR}} = 0.6$ . We assume that the pump and the Stokes beams propagate along the  $+z$  direction and that the signal is detected in the forward direction. The pump wavelength is assumed to be 750 nm. The image intensity at each pixel was calculated by an integration of the CARS radiation field over a spherical volume with diameter  $6.0\lambda_p$  and centered at the focus.

The lateral CARS intensity profiles along the  $x$  axis of a  $1\text{-}\mu\text{m}$  scatterer are calculated with Eqs. (13) and (14) and are shown in Fig. 6(a) as a function of the detuning  $(\omega_p - \omega_s) - \omega_R$ . It is interesting that the image contrast becomes much lower when  $\omega_p - \omega_s$  is positively detuned from the vibrational frequency by several wave numbers. This occurs as a result of destructive interference between the resonant signal from the scatterer and the nonresonant signal from the solvent and the scatterer, which is consistent with the characteristic dip in a CARS spectrum<sup>31</sup> [see Fig. 8(a) below, for example]. The highest image contrast is obtained with a small negative detuning, in accordance with the redshift of the CARS peak from the central frequency of the spontaneous Raman band. When  $\omega_p - \omega_s$  is tuned away from any Raman resonance, the contrast is still present as a result of the different nonresonant susceptibilities of the scatterer and the solvent. However, these effects can be circumvented with polarization-sensitive detection that suppresses the nonresonant background from both the scatterer and the solvent.

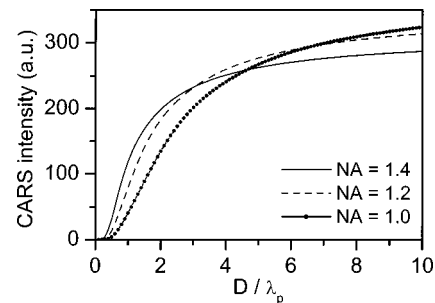


Fig. 5. Forward-detected CARS signals as a function of diameter  $D$  of a spherical scatterer calculated with copropagating pump and Stokes beams and objective lenses with different NAs.



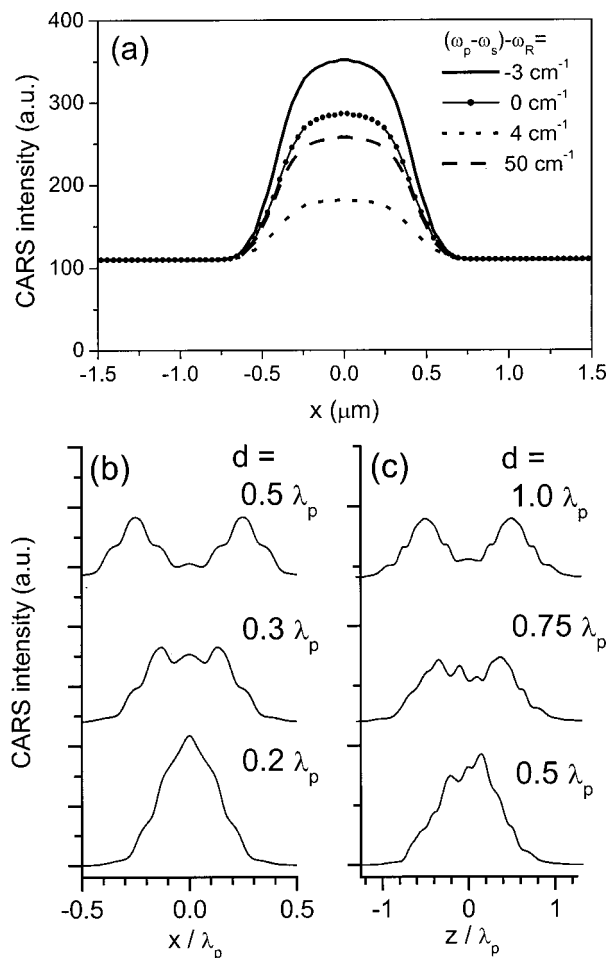


Fig. 6. (a) Lateral image intensity profile as a function of the detuning from the vibrational resonance frequency,  $(\omega_p - \omega_s) - \omega_R$ , for a  $1\text{-}\mu\text{m}$  spherical scatterer embedded in a nonlinear medium. (b), (c) Lateral and axial intensity profiles of two identical spherical scatterers with diameter  $0.2\lambda_p$  and separated by a distance  $d$  along the  $x$  and the  $z$  axes, respectively.

Next we consider two adjacent spherical samples with diameter  $0.2\lambda_p$ . For simplicity we assume that there is no background signal from the solvent. Figure 6(b) shows the lateral CARS intensity profile for the two scatterers located in the focal plane at different separation distances. The two scatterers are clearly resolvable when they are separated by  $0.5\lambda_p$ . The FWHM of  $0.25\lambda_p$  for each peak is below the diffraction limit of  $0.61\lambda_p/\text{NA}$ , owing to the nonlinear and coherent properties of CARS. It is interesting to note the intensity modulation in the profile that results from the interference between the signals of the two scatterers. At distance  $0.3\lambda_p$  the coherent superposition of the CARS signal causes the appearance of a third peak in the middle of the two peaks for each scatterer. Finally, the two scatterers cannot be resolved at all when they touch each other. In this case, only one peak shows up with a stronger intensity. Similar results are obtained in the axial direction, as shown in Fig. 6(c). However, the coherent addition in the axial direction leads to an asymmetric intensity profile when the two scatterers approach each other.

Figures 6(b) and 6(c) allow us to evaluate the spatial resolution of CARS microscopy in terms of its capability

for resolving adjacent Raman-active scatterers. It can be seen that a lateral resolution of  $0.5\lambda_p$  and a depth resolution of  $1.0\lambda_p$  can be achieved in CARS microscopy with objective lenses of 1.4 NA. Figures 6(b) and 6(c), however, imply that the coherent property of CARS can scramble the spatial resolution to some extent.

## 4. EXPERIMENTAL IMPLEMENTATION

### A. Instrumentation

We implemented CARS microscopy by using four different configurations: (a) forward-detected CARS (F-CARS) with parallel-polarized pump and Stokes beams, (b) forward-detected polarization CARS (P-CARS), (c) epide-detected CARS (E-CARS) with parallel-polarized pump and Stokes beams, and (d) counterpropagating CARS (C-CARS) with parallel-polarized pump and Stokes beams and detection in the pump beam propagation direction. Schematics of these configurations are shown in Fig. 7.

We obtained CARS images by raster scanning the sample with respect to the fixed laser beams, using a three-dimensional scanning stage (Physik Instrumente, Germany) on an inverted microscope (TE300, Nikon). The filtered CARS signal was detected with an avalanche photodiode (Perkin-Elmer, Canada). The detection area was  $\sim 170 \mu\text{m} \times 170 \mu\text{m}$ . No confocal pinholes were used for epidection. The F-CARS, E-CARS, and P-CARS images were obtained with two synchronized near-IR picosecond pulse trains at a repetition rate of 80

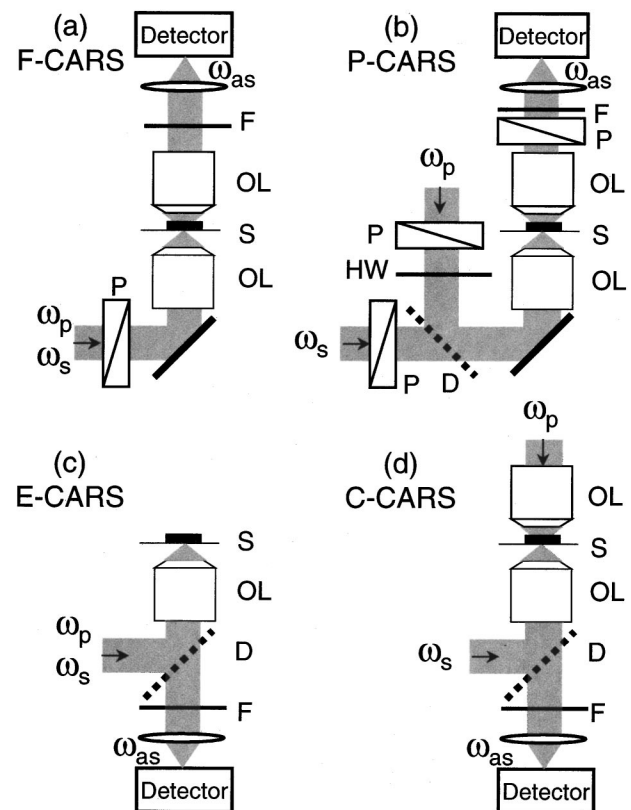


Fig. 7. Schematic of the configurations for F-CARS, P-CARS, E-CARS, and C-CARS microscopes. P's, polarizers; OL's, objective lenses; S's, samples; F's, filters; HW, half-wave plate; D's, dichroic mirrors.



MHz (Tsunami, Spectra-Physics).<sup>38</sup> The repetition rate was reduced to several hundred kilohertz by a pair of Pockels cells (Model 350-160, Conoptics). The CARS signal could be enhanced  $m^2$  times if the repetition rate was lowered by  $m$  times while the same average power was maintained. The transform-limited pulse width of each beam was 5 ps (FWHM), corresponding to a spectral width of  $2.9 \text{ cm}^{-1}$  (FWHM). The pump wavelength was tunable from 690 to 840 nm, and the Stokes beam from 770 to 900 nm. The focusing lens was either an NA = 1.2 water objective lens (Olympus) or an NA = 1.4 oil objective lens (Nikon). The collecting lens is an NA = 1.4 oil objective lens (Nikon). The C-CARS image was obtained with two identical oil objective lenses (Nikon) on a regeneratively amplified Ti:sapphire laser system that pumps an optical parametric amplifier (RegA9000/OPA9400, Coherent).<sup>39</sup> The pump and Stokes beams were two 110-fs (FWHM) pulse trains, at 800 and 917 nm, respectively, at a repetition rate of 250 kHz.

## B. Characterization

Polystyrene beads embedded in water were used as a model system. We focused on two weak Raman bands, at 1601 and  $1582 \text{ cm}^{-1}$ . These two bands correspond to the quadrant stretch of the monosubstituted benzene ring,<sup>60</sup> with intensities comparable with those of the protein and DNA Raman bands in the fingerprint region.

Figure 8(a) shows the F-CARS and spontaneous Raman spectra of polystyrene in the  $1550\text{--}1650\text{-cm}^{-1}$  region. A large nonresonant signal is present in the F-CARS spectrum. The redshift of the peaks and the dip at  $1608 \text{ cm}^{-1}$  result from the interference of the resonant and nonresonant CARS signals.<sup>31</sup> Figures 8(b)–8(e) show the F-CARS images of  $1\text{-}\mu\text{m}$  polystyrene beads in water. The lateral intensity profile across the bead is shown below each image. A large background signal from water is present in all the F-CARS images. The dependence of the image contrast on the detuning is consistent with our calculation [Fig. 6(a)]. As shown in Fig. 8(b), the highest image contrast is obtained with small negative detuning, in agreement with the shift of the CARS band peak toward lower frequency. The image contrast becomes much lower when  $\omega_p - \omega_s$  is positively detuned from the vibrational frequency by several wave numbers [Fig. 8(d)]. This lower image contrast arises from the destructive interference between the signal from the bead and that from water and is consistent with the characteristic dip at  $1608 \text{ cm}^{-1}$  of the CARS spectrum. When  $\omega_p - \omega_s$  is tuned away from any Raman resonance [Fig. 8(e)], the contrast is still present owing to the nonresonant contributions of the polystyrene beads.

It is interesting that the F-CARS images in Figs. 8(b)–8(e) show a weak dip about the beads (see the dip at the distance of  $3.5 \mu\text{m}$  in the intensity profile). The dip might be the result of destructive interference between the CARS field from the scatterer and that from the surrounding solvent. Another reason for the dip might be the mismatch of the index of refraction between the scatterer and the solvent, which distorts the foci of the excitation fields and reduces the forward-detected signal.

High vibrational contrast was obtained by P-CARS microscopy by efficient suppression of the nonresonant back-

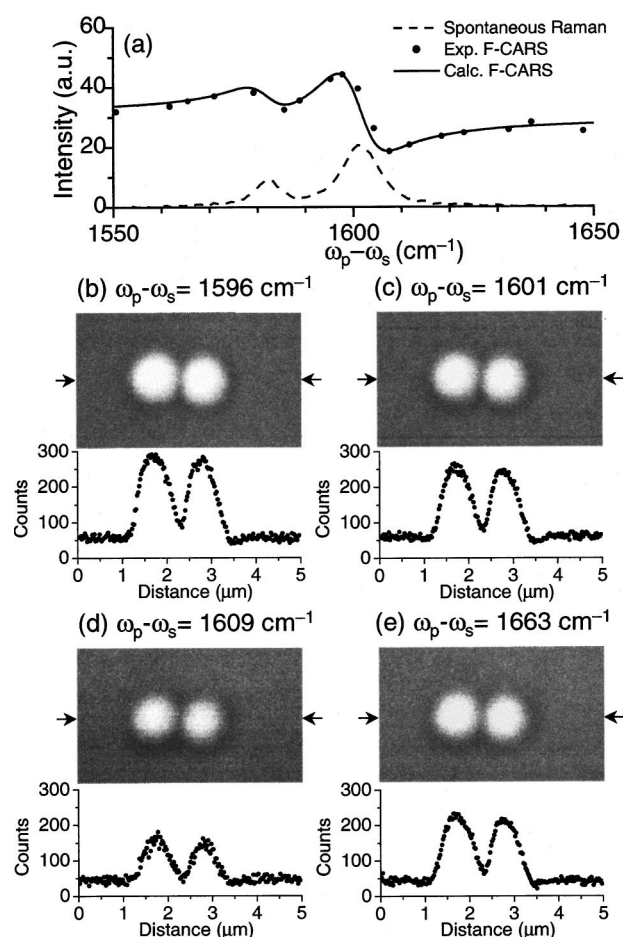


Fig. 8. (a) F-CARS and spontaneous Raman spectra of a polystyrene film spin coated onto a coverslip. The F-CARS spectrum was taken with an average pump power of  $780 \mu\text{W}$  and an average Stokes power of  $390 \mu\text{W}$  at a repetition rate of 100 kHz. The pump frequency was fixed at  $13\,325 \text{ cm}^{-1}$ . The Raman spectrum was recorded on a Raman spectrometer (Jobin-Yvon-Spec, LabRam). The F-CARS spectrum (solid curve) was simulated by Eq. (16). The parameters for the two Raman bands were set as  $\omega_1 = 1601 \text{ cm}^{-1}$ ,  $\omega_2 = 1582 \text{ cm}^{-1}$ ,  $\Gamma_1 = \Gamma_2 = 3.5 \text{ cm}^{-1}$ ,  $A_2/A_1 = 0.3$ , and  $\chi_{\text{NR}}^{(3)}/A_1 = 0.55 \text{ cm}$ . The pulse widths of the pump and the Stokes beams were chosen to be  $2.9 \text{ cm}^{-1}$ . Shown below the spectra are the F-CARS images of  $1\text{-}\mu\text{m}$  polystyrene beads upon a coverslip and covered with water. The pump and Stokes powers were 0.6 and 0.3 mW, respectively, at a repetition rate of 400 kHz. The size of each image was  $5 \mu\text{m} \times 3 \mu\text{m}$ , and the acquisition time was 96 s for each image.

ground from the scatterer and the solvent. For the 1582- and  $1601\text{-cm}^{-1}$  bands of polystyrene the depolarization ratio was measured with a Raman spectrometer (Jobin-Yvon-Spec; LabRam) to be 0.71. An extinction ratio of 600 for the nonresonant CARS signal was achieved with NA = 1.4 objective lenses. Thus the contrast can be enhanced by a factor of 150 according to Eq. (21).

Figure 9(a) shows the P-CARS spectrum of polystyrene. It is evident that the nonresonant background is effectively suppressed and that the P-CARS peaks coincide with the spontaneous Raman peaks. Shown below the spectrum are three P-CARS images, at 1582, 1600, and  $1652 \text{ cm}^{-1}$ , of the same  $1\text{-}\mu\text{m}$  polystyrene beads spin coated onto a coverslip and covered with water. The lateral intensity profile across the bead is shown below each

image. Efficient reduction of the nonresonant water signal results in a signal-to-background ratio of better than 50:1 [Fig. 9(c)], which is much higher than that in the F-CARS image with parallel-polarized incident beams (Fig. 8). It should be noted that no P-CARS signal from the weak Raman band of water near  $1620\text{ cm}^{-1}$  was detected. The ratio of the peak intensity with  $\omega_p - \omega_s = 1600\text{ cm}^{-1}$  [Fig. 9(c)] to that with  $\omega_p - \omega_s = 1582\text{ cm}^{-1}$  [Fig. 9(b)] is about 2:1, consistent with the P-CARS spectrum of polystyrene shown above the images. When  $\omega_p - \omega_s$  was off resonant ( $1652\text{ cm}^{-1}$ ), the signal shown in Fig. 9(d) was 20 times weaker than that with  $\omega_p - \omega_s$  tuned to  $1600\text{ cm}^{-1}$ . We believe that this residual contrast results from the birefringence of both the excitation and the signal fields induced at the nonplanar and index-mismatched interface between polystyrene beads and water, similar to the contrast mechanism of polarization microscopy. This contrast has no spectral selectivity, and one can distinguish it from the vibrational contrast in a P-CARS image by tuning  $\omega_p - \omega_s$  away from the Raman resonance. With  $\omega_p - \omega_s$  tuned to the  $1000\text{-cm}^{-1}$  band, 200-nm polystyrene beads embedded in gel could be detected with a signal-to-background ratio of 5:1 in our experiment.

High-sensitivity imaging of small features was achieved with E-CARS microscopy by significant reduction of the solvent background signal. Figure 10(a) shows an E-CARS image of three adjacent 200-nm polystyrene beads embedded in 2% agarose gel.  $\omega_p - \omega_s$  was tuned to the aromatic C—H vibration at  $3052\text{ cm}^{-1}$ . A signal-to-background ratio of  $\sim 40:1$  was obtained. The source of the background is the dark counts. The back-

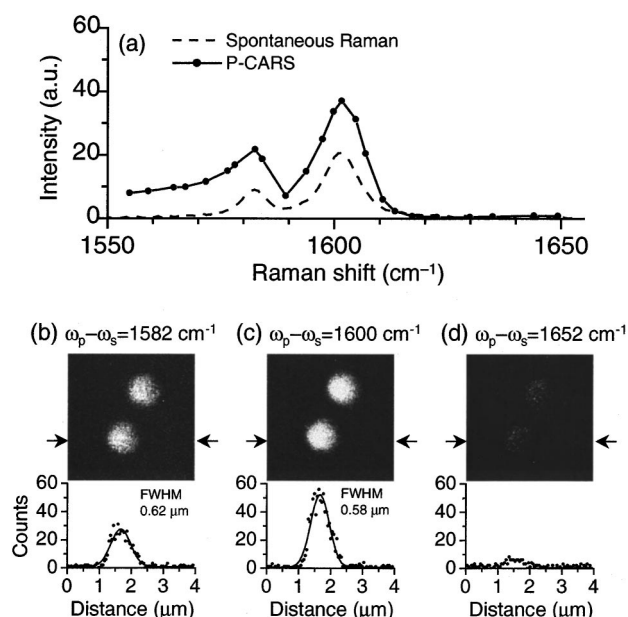


Fig. 9. (a) P-CARS spectrum of a polystyrene film taken at an average pump power of 2 mW and an average Stokes power of 1 mW at a repetition rate of 400 kHz. The pump frequency was fixed at  $13\,325\text{ cm}^{-1}$ . Shown below the spectrum are P-CARS images of  $1\text{-}\mu\text{m}$  polystyrene beads upon a coverslip and covered with water. The pump and Stokes powers were 1.2 and 0.6 mW, respectively, at a repetition rate of 400 kHz. The size of the image was  $4\text{ }\mu\text{m} \times 4\text{ }\mu\text{m}$ , and the acquisition time was 160 s for each image.

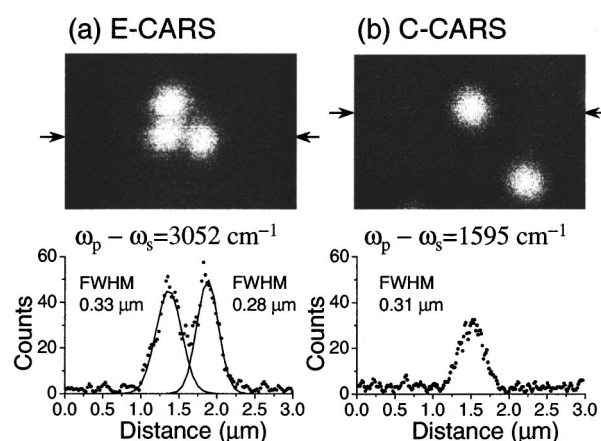


Fig. 10. (a) E-CARS image of  $0.2\text{-}\mu\text{m}$  beads embedded in 2% agarose gel; pump frequency,  $14\,183\text{ cm}^{-1}$ . The pump and Stokes powers were 2.5 and 1.8 mW at an 800-kHz repetition rate. The image size was  $3\text{ }\mu\text{m} \times 2\text{ }\mu\text{m}$ , and the acquisition time was 80 s. (b) C-CARS image of  $0.5\text{-}\mu\text{m}$  beads in water. The pump and Stokes beams were two 110-fs pulse trains at 800 and 917 nm, respectively. The pump and Stokes powers were 100 and 50  $\mu\text{W}$ , respectively, at a repetition rate of 250 kHz. The image size was  $3\text{ }\mu\text{m} \times 2\text{ }\mu\text{m}$ , and the acquisition time was 126 s.

ward CARS signal from bulk water was undetectable in our experiment. The undetected signal from the polystyrene beads resulted from a lack of destructive interference of the backward CARS because the bead size was much smaller than the excitation wavelength. As the pump wavelength used for this image was 710 nm, the bead diameter of 200 nm was near  $0.3\lambda_p$ , where the first maximum of the E-CARS signal was reached [see Fig. 4(a)].

The lateral intensity profile in Figure 10(a) shows that the adjacent  $0.2\text{-}\mu\text{m}$  beads separated by  $0.5\text{ }\mu\text{m}$  can be clearly resolved, indicating a lateral resolution of better than  $0.5\text{ }\mu\text{m}$ . By moving a water objective lens (NA = 1.2) with a stepping motor, we obtained the axial CARS intensity profile of a 200-nm polystyrene bead, with a FWHM of 750 nm (data not shown). This result indicates that the axial resolution of CARS microscopy is  $\sim 1.0\lambda_p$  under the tight-focusing condition.

C-CARS microscopy provides another way to image submicrometer features embedded in a nonlinear medium with high sensitivity. Figure 10(b) shows a C-CARS image of 500-nm beads upon a cover glass and covered with water.  $\omega_p - \omega_s$  was tuned to the Raman band at  $1600\text{ cm}^{-1}$ . A signal-to-background ratio of  $\sim 10:1$  was obtained by effective suppression of the background signal from the surrounding bulk medium. Compared to that in E-CARS, implementation of the spatial overlap of the two foci of the pump and Stokes beams is more difficult in C-CARS microscopy.

### C. Live Cell Imaging

Chemical mapping of living cells is one of the major applications of CARS microscopy. It is useful to compare the performance of F-CARS, E-CARS, and P-CARS in live cell imaging. Figure 11 shows the F-CARS, E-CARS, and

P-CARS images of unstained epithelial cells with  $\omega_p - \omega_s$  tuned to the fingerprint region of the Raman spectra of biological molecules.

F-CARS necessitates using low excitation power. However, the F-CARS signals from the cellular components are overwhelmed by the large water background, as can be seen from the intensity profile below the image.

E-CARS greatly improves the image contrast by means of efficient suppression of the water background.<sup>38,39</sup> Epidetection, however, cannot discriminate the nonresonant background from the scatterers. The spectral selectivity of E-CARS microscopy is poor when the nonresonant signal from  $\chi_{\text{sca}}^{(3)\text{NR}} - \chi_{\text{sol}}^{(3)\text{NR}}$  exceeds the resonant signal from  $\chi_{\text{sca}}^{(3)\text{R}}$ . E-CARS can be used for vibrational imaging with strong resonant CARS signals, for example, imaging of live cells based on the C—H stretching vibra-

tion when the resonant signal is much larger than the nonresonant background because of the high density of the C—H modes.

P-CARS can suppress the nonresonant background from both the scatterers and the solvent. Figure 11(c) shows the distribution of proteins in an epithelial cell based on the P-CARS contrast of the amide I band.<sup>40</sup> Detuning  $\omega_p - \omega_s$  from the amide I band results in faint contrast, which proves the spectral selectivity. The background shown in the intensity profile of Fig. 11(c) arises from leakage of the excitation beams and the residual nonresonant signal.

## 5. CONCLUSIONS

In this paper we have presented a systematic theoretical description and experimental characterization of CARS microscopy. We have developed a theoretical model of CARS signal generation from an arbitrary Raman scatterer by tightly focused Gaussian beams based on the Green's function method. This model is generally applicable to signal generation in any nonlinear coherent microscopy. Our calculations provide a quantitative description of the contrast mechanisms and the imaging properties of CARS microscopy.

CARS imaging is distinctively different from fluorescence imaging because of its coherent nature. Coherent summation of CARS from different parts of the sample and the interference between resonant and nonresonant CARS signals determine the image intensity. Our experimental results demonstrate that collinear CARS microscopy gives a lateral resolution of better than  $0.5 \mu\text{m}$  and a depth resolution of  $0.75 \mu\text{m}$  with tightly focused excitation beams.

F-CARS microscopy produces a large signal at low excitation power. However, the resonant F-CARS signal is often overwhelmed by the nonresonant background from the scatterers and the solvent. The E-CARS and C-CARS beam geometries introduce a phase mismatch, which acts as a size filter that effectively rejects the signal from the bulk solvent. E-CARS and C-CARS signals arise from small scatterers or from interfaces of two sizable media that have different values of  $\chi^{(3)}$ . The E-CARS signal could be complicated by backreflection of the forward CARS signal at an interface. C-CARS avoids the backreflection problem, but its implementation is more difficult. P-CARS microscopy efficiently reduces the nonresonant background from both the scatterers and the solvent. In practice, the scatterers could induce some birefringence for the excitation field and the signal field and produce an additional contrast [see Fig. 9(d)] that is frequency independent and can be distinguished from the vibrational contrast by tuning of the laser frequency.

The various beam geometries and detection schemes described in this paper can be applied under different circumstances. F-CARS is suitable for vibrational imaging based on certain modes (e.g., C—H stretching vibration) with a large resonant CARS signal. P-CARS provides a general method of vibrational imaging with high contrast. E-CARS permits high-sensitivity imaging of small features embedded in a nonlinear medium. Our experimental implementation has demonstrated the exciting possi-

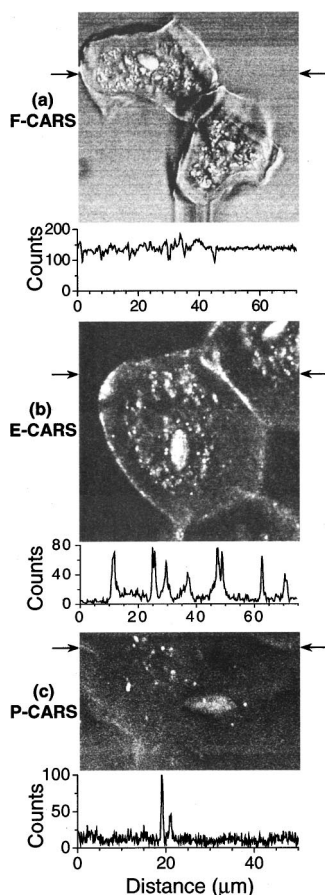


Fig. 11. (a) F-CARS image of unstained epithelial cells.  $\omega_p - \omega_s$  was tuned to  $1579 \text{ cm}^{-1}$ , with the pump frequency at  $13330 \text{ cm}^{-1}$ . The pump and Stokes powers were 0.4 and 0.2 mW at a 400-kHz repetition rate. The image size was  $72 \mu\text{m} \times 72 \mu\text{m}$ , and the acquisition time was 12 min. (b) E-CARS image of unstained epithelial cells.  $\omega_p - \omega_s$  was tuned to  $1570 \text{ cm}^{-1}$ , with the pump frequency at  $13333 \text{ cm}^{-1}$ . The pump and Stokes powers were 2.0 and 1.0 mW at a 400-kHz repetition rate. The image size was  $75 \mu\text{m} \times 75 \mu\text{m}$ , and the acquisition time was 12 min. (c) P-CARS image of an unstained epithelial cell.  $\omega_p - \omega_s$  was tuned to  $1650 \text{ cm}^{-1}$ , with the pump frequency at  $13324 \text{ cm}^{-1}$ . The pump and Stokes powers were 1.8 and 1.0 mW at a 400-kHz repetition rate. The image size was  $50 \mu\text{m} \times 30 \mu\text{m}$ , and the acquisition time was 8 min. Shown below each image is the intensity profile along the line indicated by the two arrows.



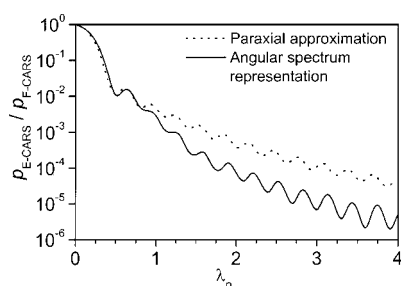


Fig. 12. Calculated ratio of forward to backward CARS radiation power as a function of diameter  $D$  for a spherical sample centered at the focus. The tightly focused field ( $\text{NA} = 1.4$ ) was calculated from the angular spectrum representation [Eq. (4)] and from the paraxial approximation [Eq. (A1)].

bilities of high-sensitivity and noninvasive chemical mapping of living cells and composite materials by CARS microscopy.

## APPENDIX A

In this appendix we check quantitatively the difference between the paraxial approximation and the angular spectrum representation in calculations of nonlinear optical signal generation. Under the paraxial approximation, the focus field for a fundamental Gaussian beam at wavelength  $\lambda$  is given by<sup>46</sup>

$$E(\rho, z) = E_0 \frac{w_0}{w(z)} \exp\left[-\frac{\rho^2}{w(z)^2}\right] \times \exp\left\{i\left[kz - \eta(z) + \frac{k\rho^2}{2R(z)}\right]\right\}, \quad (\text{A1})$$

where  $w(z) = w_0(1 + z^2/z_0^2)^{1/2}$  is the beam waist,  $R(z) = z(1 + z_0^2/z^2)^{1/2}$  is the wave-front radius,  $\eta(z) = \arctan(z/z_0)$  is the Gouy phase shift, and  $z_0 = kw_0^2/2$  is the Rayleigh range.  $w_0$  is calculated as  $0.61\lambda/(\text{NA}\sqrt{2 \ln 2})$ , where  $\text{NA} = 1.4$ . The ratio of forward- to backward-detected CARS signals for a sphere centered at the focus calculated with Eq. (A1) and that with Eq. (4) is shown in Fig. 12. The two curves overlap for small samples with diameters smaller than  $0.75 \lambda_p$ . However, a large difference shows up for large samples. As the E-CARS signal from bulk is not detectable in our experiment, the calculation with an angular spectrum representation gives a better description of the experimental observation.

## ACKNOWLEDGMENTS

This study was supported by National Institutes of Health grant GM62536-01 and by a start-up fund at Harvard University. The authors thank the Harvard Materials Research Science and Engineering Center (grant NSF DMR-9809363) for partial support of instrumentation, Lukas Novotny for sharing the theoretical description of tightly focused Gaussian fields and for comments on the manuscript, Lewis Book for helpful discussions, Erik Sánchez for technical assistance, and Hiroko Miki for measuring the Raman depolarization ratio of polysty-

rene. A. Volkmer acknowledges support from the Deutsche Forschungsgemeinschaft.

\*Present address: 3 Physikalisches Institut, Universität Stuttgart, Pfaffenwaldring 57, 70550 Stuttgart, Germany. Sunney Xie's email address is xie@chemistry.harvard.edu.

## REFERENCES AND NOTES

1. E. Kohen and J. G. Hirschberg, *Cell Structure and Function by Microspectrofluorometry* (Academic, San Diego, Calif., 1989).
2. J. B. Pawley, *Handbook of Biological Confocal Microscopy* (Plenum, New York, 1995).
3. R. P. Haugland, *Handbook of Fluorescent Probes and Research Chemicals*, 6th ed. (Molecular Probes, Eugene, Ore., 1996).
4. T. Wilson and C. Sheppard, *Theory and Practice of Scanning Optical Microscopy* (Academic, Orlando, Fla., 1984).
5. W. Denk, J. H. Strickler, and W. W. Webb, "Two-photon laser scanning fluorescence microscopy," *Science* **248**, 73–76 (1990).
6. C. Xu, W. Zipfel, J. B. Shear, R. M. Williams, and W. W. Webb, "Multiphoton fluorescence excitation: new spectral windows for biological nonlinear microscopy," *Proc. Natl. Acad. Sci. U.S.A.* **93**, 10,763–10,768 (1996).
7. M. Straub, P. Lodemann, P. Holroyd, R. Jahn, and S. W. Hell, "Live cell imaging by multifocal multiphoton microscopy," *Eur. J. Cell. Biol.* **79**, 726–734 (2000).
8. J. Hoyland, "Fluorescent probes in practice—potential artifacts," in *Fluorescent and Luminescent Probes for Biological Activity*, W. T. Mason, ed. (Academic, San Diego, Calif., 1999), p. 108.
9. H. J. Humecki, *Practical Guide to Infrared and Microspectroscopy*, Vol. 19 of *Practical Spectroscopy*, E. G. Brame, Jr., ed. (Marcel Dekker, New York, 1995).
10. G. Turrell and J. Corset, *Raman Microscopy Development and Applications* (Academic, San Diego, Calif., 1996).
11. N. M. Sijtsema, S. D. Wouters, C. J. de Grauw, C. Otto, and J. Greve, "Confocal direct imaging Raman microscope: design and applications in biology," *Appl. Spectrosc.* **52**, 348–355 (1998).
12. R. J. H. Clark and R. E. Hester, eds., *Advances in Nonlinear Spectroscopy* (Wiley, New York, 1988), Vol. 15.
13. P. D. Maker and R. W. Terhune, "Study of optical effects due to an induced polarization third order in the electric field strength," *Phys. Rev.* **137**, A801–A818 (1965).
14. Y. R. Shen, *The Principles of Nonlinear Optics* (Wiley, New York, 1984).
15. M. D. Levenson and S. S. Kano, *Introduction to Nonlinear Laser Spectroscopy* (Academic, San Diego, Calif., 1988).
16. S. Velsko and R. M. Hochstrasser, "Studies of vibrational relaxation in low-temperature molecular crystal using coherent Raman spectroscopy," *J. Phys. Chem.* **89**, 2240–2253 (1985).
17. R. Gauderon, P. B. Lukins, and C. J. R. Sheppard, "Three-dimensional second-harmonic generation imaging with femtosecond laser pulses," *Opt. Lett.* **23**, 1209–1211 (1998).
18. P. J. Campagnola, M.-D. Wei, A. Lewis, and L. M. Loew, "High-resolution nonlinear optical imaging of live cells by second harmonic generation," *Biophys. J.* **77**, 3341–3349 (1999).
19. L. Moreaux, O. Sandre, and J. Mertz, "Membrane imaging by second-harmonic generation microscopy," *J. Opt. Soc. Am. B* **17**, 1685–1694 (2000).
20. M. Florsheimer, C. Brillert, and H. Fuchs, "Chemical imaging of interfaces by sum frequency microscopy," *Langmuir* **15**, 5437–5439 (1999).
21. Y. Barad, H. Eisenberg, M. Horowitz, and Y. Silberberg, "Nonlinear scanning laser microscopy by third-harmonic generation," *Appl. Phys. Lett.* **70**, 922–924 (1997).

22. M. Müller, J. Squier, K. R. Wilson, and G. J. Brakenhoff, "3D-microscopy of transparent objects using third-harmonic generation," *J. Microsc. (Oxford)* **191**, 266–274 (1998).
23. M. D. Duncan, J. Reintjes, and T. J. Manuccia, "Scanning coherent anti-Stokes Raman microscope," *Opt. Lett.* **7**, 350–352 (1982).
24. A. Zumbusch, G. R. Holtom, and X. S. Xie, "Three-dimensional vibrational imaging by coherent anti-Stokes Raman scattering," *Phys. Rev. Lett.* **82**, 4142–4145 (1999).
25. M. Müller, J. Squier, C. A. de Lange, and G. J. Brakenhoff, "CARS microscopy with folded BOXCARS phasematching," *J. Microsc. (Oxford)* **197**, 150–158 (2000).
26. M. Hashimoto, T. Araki, and S. Kawata, "Molecular vibration imaging in the fingerprint region by use of coherent anti-Stokes Raman scattering microscopy with a collinear configuration," *Opt. Lett.* **25**, 1768–1770 (2000).
27. E. O. Potma, W. P. de Boei, and D. A. Wiersma, "Nonlinear coherent four-wave mixing in optical microscopy," *J. Opt. Soc. Am. B* **17**, 1678–1684 (2000).
28. E. O. Potma, W. P. de Boei, P. J. M. van Haastert, and D. A. Wiersma, "Real-time visualisation of intracellular hydrodynamics in single living cells," *Proc. Natl. Acad. Sci. U.S.A.* **98**, 1577–1582 (2001).
29. J. A. Shirley, R. J. Hall, and A. C. Eckbreth, "Folded BOXCARS for rotational Raman studies," *Opt. Lett.* **5**, 380–382 (1980).
30. G. C. Bjorklund, "Effects of focusing on third-order nonlinear processes in isotropic media," *IEEE J. Quantum Electron.* **QE-11**, 287–296 (1975).
31. S. Maeda, T. Kamisuki, and Y. Adachi, "Condensed phase CARS," in *Advances in Non-linear Spectroscopy*, R. J. H. Clark and R. E. Hester, eds. (Wiley, New York, 1988), p. 253.
32. R. T. Lynch, Jr., S. D. Kramer, H. Lotem, and N. Bloembergen, "Double resonance interference in third-order light mixing," *Opt. Commun.* **16**, 372–375 (1976).
33. F. M. Kamga and M. G. Sceats, "Pulse-sequenced coherent anti-Stokes Raman scattering spectroscopy: a method for suppression of the nonresonant background," *Opt. Lett.* **5**, 126–128 (1980).
34. J. J. Song, G. L. Eesley, and M. D. Levenson, "Background suppression in coherent Raman spectroscopy," *Appl. Phys. Lett.* **29**, 567–569 (1976).
35. S. A. Akhmanov, A. F. Bunkin, S. G. Ivanov, and N. I. Koroteev, "Coherent ellipsometry of Raman scattering of light," *JETP* **25**, 416–420 (1977).
36. J.-L. Oudar, R. W. Smith, and Y. R. Shen, "Polarization-sensitive coherent anti-Stokes Raman spectroscopy," *Appl. Phys. Lett.* **34**, 758–760 (1979).
37. R. Brakel and F. W. Schneider, "Polarization CARS spectroscopy," in *Advances in Non-linear Spectroscopy*, R. J. H. Clark and R. E. Hester, eds. (Wiley, New York, 1988), p. 149.
38. J. X. Cheng, A. Volkmer, L. D. Book, and X. S. Xie, "An epidected coherent anti-Stokes Raman scattering (E-CARS) microscope with high spectral resolution and high sensitivity," *J. Phys. Chem. B* **105**, 1277–1280 (2001).
39. A. Volkmer, J.-X. Cheng, and X. S. Xie, "Vibrational imaging with high sensitivity via epidected coherent anti-Stokes Raman scattering microscopy," *Phys. Rev. Lett.* **87**, 0239011–0239014 (2001).
40. J. X. Cheng, L. D. Book, and X. S. Xie, "Polarization coherent anti-Stokes Raman scattering microscopy," *Opt. Lett.* **26**, 1341–1343 (2001).
41. W. M. Shaub, A. B. Harvey, and G. C. Bjorklund, "Power generation in coherent anti-Stokes Raman spectroscopy with focused laser beams," *J. Chem. Phys.* **67**, 2547–2550 (1977).
42. S. G. Guha and J. Falk, "The effects of focusing on the efficiency of coherent anti-Stokes Raman scattering," *J. Chem. Phys.* **75**, 2599–2562 (1981).
43. L. C. Davis, K. A. Marko, and L. Rimai, "Angular distribution of coherent Raman emission in degenerate four-wave mixing with pumping by a single diffraction coupled laser-beam: configurations for high spatial resolution," *Appl. Opt.* **20**, 1685–1690 (1981).
44. R. E. Teets, "CARS signals: phase matching, transverse modes, and optical damage effects," *Appl. Opt.* **25**, 855–862 (1986).
45. W. Kaabar and R. Devonshire, "A versatile model of CARS signal generation: optimum beam diameter ratios for different phase-matching geometries," *Chem. Phys. Lett.* **186**, 522–530 (1991).
46. A. E. Siegman, *Lasers* (University Science Books, Mill Valley, Calif., 1986).
47. B. Richards and E. Wolf, "Electromagnetic diffraction in optical systems. II. Structure of the image field in an aplanatic system," *Proc. R. Soc. London, Ser. A* **253**, 358–379 (1959).
48. L. Novotny, *Lecture Notes on "Nano-Optics"* (University of Rochester, Rochester, N.Y., 2000).
49. The most significant term for CARS radiation involving the  $z$ -polarized field is  $\chi_{zzxz}^{(3)} E_p^x E_p^x (E_s^z)^*$ , which is  $\sim 1\%$  of  $\chi_{xxxx}^{(3)} E_p^x E_p^x (E_s^x)^*$  with  $\chi_{zzxz}^{(3)} = \chi_{xxxx}^{(3)}/3$ . Thus the radiation power from the former term is only 0.01% of that from the latter term. Moreover, the radiation from the former term is maximized in the  $z = 0$  plane, so little signal can be detected in the forward or the backward direction. Experimentally, we observed that the nonresonant CARS signal was highly polarized along the same direction as the parallel-polarized pump and Stokes beams. This observation verifies the validity of our assumption.
50. H. Ling and S. W. Lee, "Focusing of electromagnetic waves through a dielectric interface," *J. Opt. Soc. Am. A* **1**, 965–973 (1984).
51. S. Hell, G. Reiner, C. Cremer, and E. H. K. Stelzer, "Aberrations in confocal fluorescence microscopy induced by mismatches in refractive index," *J. Microsc. (Oxford)* **169**, 391–405 (1993).
52. R. W. Boyd, *Nonlinear Optics* (Academic, Boston, Mass., 1992).
53. S. Mukamel, *Principles of Nonlinear Optical Spectroscopy* (Oxford U. Press, New York, 1995).
54. W. C. Chew, *Waves and Fields in Inhomogeneous Media*, 2nd ed. (Institute of Electrical and Electronics Engineers, New York, 1995).
55. L. Novotny, "Allowed and forbidden light in near-field optics. II. Interacting dipolar particles," *J. Opt. Soc. Am. A* **14**, 105–113 (1997).
56. H. Lotem, R. T. Lynch, Jr., and N. Bloembergen, "Interference between Raman resonances in four-wave difference mixing," *Phys. Rev. A* **14**, 1748–1755 (1976).
57. D. A. Kleinman, "Nonlinear dielectric polarization in optical media," *Phys. Rev.* **126**, 1977–1979 (1962).
58. M. A. Yuratich and D. C. Hanna, "Coherent anti-Stokes Raman spectroscopy (CARS) selection rules, depolarization ratios and rotational structure," *Mol. Phys.* **33**, 671–682 (1977).
59. As our calculation did not consider the contribution from the solvent surrounding the scatterer, the forward radiation pattern is a suitable description of polarization CARS for which the nonresonant background from the solvent is suppressed. The forward CARS generated by a pair of parallel-polarized pump and Stokes beams is a coherent addition of the signal from the scatterer and that from the solvent and is always highly directional.
60. D. Lin-Vien, N. B. Colthup, W. G. Fateley, and J. G. Grasselli, *Handbook of Infrared and Raman Characteristic Frequencies of Organic Molecules* (Academic, San Diego, Calif., 1991).